1   **Evolution of immune escape mechanisms in the progression from preinvasive to**
2   **invasive human lung adenocarcinoma.**

3   Nasser K. Altorki[*,1,2,3], Alain C. Borczuk[3,4], Vivek Mittal[1,2,3,5], Olivier Elemento [3,6], and Timothy E.
4   McGraw[*,1,3,7]

5   [1] Department of Cardiothoracic Surgery, Weill Cornell Medicine and NY Presbyterian Hospital,
6   New York, NY.

7   [2] Neuberger Berman Foundation Lung Cancer Research Center, Weill Cornell Medicine and NY
8   Presbyterian Hospital, New York, NY.

9   [3] Meyer Cancer Center, Weill Cornell Medicine and NY Presbyterian Hospital, New York, NY.

10 [4] Department of Pathology, Weill Cornell Medicine and NY Presbyterian Hospital

11 [5] Department of Cell Biology, Weill Cornell Medicine New York, NY.

12 [6] Caryl and Israel Englander Institute for Precision Medicine, Institute for Computational
13   Biomedicine, Department of Physiology and Biophysics, Weill Cornell Medicine

14 [7] Department of Biochemistry, Weill Cornell Medicine, New York, NY.

15
16 *co-corresponding authors:
17 Nasser K Altorki
18   525 East 68th Street
19   Room M404
20   New York, NY 10065
21   T: 212 746-5156
22   F: 212 746-8223
23   NKA: nkaltork@med.cornell.edu
24
25 Timothy E McGraw
26   1300 York Ave
27   Room W305
28   New York, NY 10065
29   T: 212 746-4982
30   TEM: temcgraw@med.cornell.edu
31

32 Statement of Significance: Using multiplexed IF, we compared the cellular composition and
33 activation state of the tumor immune microenvironment between pre/minimally invasive and frankly
34 invasive adenocarcinoma. We found a progressive increase in immunosuppressive mechanisms in
35 association with disease progression suggesting that Interception strategies should be specifically
36 tailored based on underlying immune escape mechanisms
37
38 Abbreviations: TME, tumor microenvironment; LUAD, lung adenocarcinoma; p-NS, Pure non-
39 solid; AIS, adenocarcinoma *in-situ*; MIA, minimally invasive adenocarcinoma; GZB, granzyme B;
40 ROI, region of interest; CT, computer tomography; EGFR, EGF receptor; TMA, tumor
41 microenvironment.
42
43 Running title: Evolution of immune escape mechanisms in lung adenocarcinoma
44 Word count: Main text, 5560 words.
45 Figures: 7 in main text. Tables: 2 supplemental tables.

Summary

The tumor microenvironment (TME) of lung adenocarcinoma (LUAD) precursor lesions has not been described. We interrogated by multiplex immunofluorescence the TME of preinvasive and invasive Stage 1A LUADs selected by computer tomography (CT) scan-density. Pure non-solid (p-NS) CT density nodules are preinvasive/minimally invasive, whereas solid CT density nodules are frankly invasive cancers. Our data reveal an intensely immune-suppressive immune TME in p-NS tumors characterized by an increase in Treg cells and a decrease in cytotoxic T cells relative to normal lung. The TME of the solid tumor group, more advanced lesions than the p-NS yet still early in disease development, were increasingly more immune-suppressive. Provocatively, there was a further increase in both Treg cells and cytotoxic T cells, establishing a nascent albeit ineffective anti-tumor immune response in transition from preinvasive p-NS to invasive solid tumors. Regulatory T cells play a dominant role throughout progression, while additional immune evasive mechanisms are employed at different stages of disease progression, including T cell exclusion from cancer cell nests early and activation of immune checkpoints later. Our study establishes that different immune-targeted strategies are required to intercept disease progression at these two distinct early points of lung cancer development.

INTRODUCTION

The widespread use of computerized chest tomography (CT), particularly for lung cancer screening purposes, has led to the detection of ground-glass or non-solid nodules that are not visible on plain chest radiography. Non-solid nodules appear on CT scanning as hazy opacities that do not obscure the underlying lung parenchyma or vasculature. In most instances, non-solid nodules less than 5 mm in size represent focal proliferative lesions known as atypical alveolar hyperplasia that are considered the earliest progenitor lesions of invasive adenocarcinoma of the lung. The majority of non-solid nodules, particularly those ≤ 3cm in size, typically harbor adenocarcinoma *in-situ* (AIS) or minimally invasive adenocarcinoma (MIA) where the invasive component is ≤ 5 mm or less. Interestingly, 10-20% contain adenocarcinoma with an invasive component exceeding 5 mm suggestive of a more aggressive phenotype. Regardless, the precise biological behavior of these non-solid nodules remains unclear as many remain unchanged in size and appearance for many years. However, approximately 20-40% of these nodules grow or develop areas of increased CT density (a manifestation of more invasive malignancy) within a four-year window (1). Why some of these nodules retain an indolent behavior while others progress to invasive malignancy is unclear. This uncertainty commits patients to frequent, repeat imaging, and in some cases potentially harmful biopsies.

The critical role of the tumor microenvironment (TME) in tumorigenesis is well-recognized (2-5). The TME is predominantly composed of immune cells, fibroblasts and vasculature. There are a number of non-mutually exclusive hypotheses for how the TME contributes to tumorigenesis, one of which is "immunoediting" or "immune surveillance", a cancer cell-extrinsic mechanism that is engaged once cell-intrinsic killing mechanisms (e.g., apoptosis) have failed to eliminate individual transformed cells (6-8). The proposed temporal phases of cancer immune surveillance describing the homeostasis between cancer cell killing and survival include: elimination, equilibrium and escape (9). In the elimination phase, innate and adaptive immunity eliminate cancer cells before a tumor can emerge. In the equilibrium phase, immune cell killing of cancer cells is balanced by cancer cell proliferation, such that tumor growth is maintained in check, but the cancer cells are not fully eliminated. The escape phase is one of tumor growth due to cancer cells evading immune cell-mediated killing. Entry into the escape phase portends disease progression.

There are multiple mechanisms that may contribute to tumor progression, including the development of an overall immunosuppressive state in the TME and/or cancer cell driven escape mechanisms such as antigen loss or aberrations that impede antigen presentation such

3

97 as downregulation of MHC class I or II molecules. Another mechanism invoked for immune

98 evasion is T cell exclusion from cancer cell nests attributed to organized fibroblastic proliferation

99 leading to physical and/or chemical barriers that restrict access of T cells to the cancer cell

100 nests. Any or all of the above mechanisms of immune escape may contribute to tumor

101 progression in a temporal and context dependent manner.

102 We posited that progression of lung cancer from preinvasive to invasive adenocarcinoma

103 develops as a result of immune escape mediated by a shift towards a more immune-

104 suppressive microenvironment. To test this hypothesis, we used multiplex immunofluorescence

105 to compare the cellular compositions and activation states of the TMEs of radiographically pure

106 non-solid nodules (preinvasive or minimally invasive lung cancer) to the TMEs of

107 radiographically solid (invasive lung cancer) nodules. Given the importance of CT appearance in

108 driving clinical decisions in management of lung nodules, we classified the groups based on

109 their radiographic appearance (10). Comparison of these two tumor groups captures changes

110 in the TME correlated with progression from preinvasive pure non-solid (p-NS) to invasive solid

111 tumors. The characteristics of the TMEs of both p-NS and solid tumors are progressively more

112 immune suppressive than adjacent normal lung. Our findings demonstrate a diversity of

113 immune escape mechanisms at different phases during early development of human lung

114 adenocarcinoma (LUAD).

Methods

115 **Methods**

116 <u>Samples and Tissue microarray.</u> The samples for this IRB approved study were collected from

117 the Weill Cornell lung nodule cohort, a retrospective collection of CT-imaged nodules with

118 subsequent surgical resection and storage as formalin-fixed paraffin-embedded tissue. CT

119 images were reviewed by 2 observers and classified as pure non-solid or solid nodules on CT

120 attenuation. The corresponding surgical resections were reviewed for pathology, and invasion

121 was measured using Aperio whole scanned slides. Faxitron x-ray of the paraffin blocks was

122 used to identify the areas of lowest and highest tissue density for punch samples. Tissue

123 microarrays slides of 3 ROIs (1 mm diameter punch cores) per samples were generated.

124 Normal tissue was obtained from separate paraffin blocks of tissue taken away from the tumor

125 mass. The manual tissue arrayer (Beecher Instruments, Sun Prairie, WI) was used to generate

126 tissue microarray (TMA) slides.

127 <u>Multiplex imaging.</u> The immunofluorescence imaging was performed using the Neogenomics

128 platform as previously described (11). Briefly, formalin-fixed paraffin-embedded tissue arrays

129 were baked at 65°C for 1 h. Slides were deparaffinized with xylene, rehydrated by decreasing

130 ethanol concentration washes, and then processed for antigen retrieval. A two-step antigen

131 retrieval was adopted to allow antibodies with different antigen retrieval conditions to be used

132 together on the same samples (12). Samples were then blocked against nonspecific binding

133 with 10% (wt/vol) donkey serum and 3% (wt/vol) bovine serum albumin (BSA) in phosphate-

134 buffered solution (PBS) for 1 h at room temperature and stained with DAPI for 15 min. Directly

135 conjugated primary antibodies were diluted in PBS supplied with 3% (wt/vol) BSA to optimized

136 concentrations and applied for 1 h at room temperature on a Leica Bond III Stainer. In the case

137 of primary-secondary antibody staining, samples were incubated with primary antibody, followed

138 by incubation with species-specific secondary antibodies conjugated to either Cyanine 3 (cy3) or

139 cyanine 5 (cy5).

140 Stained images were collected on INCell analyzer 2200 microscope (GE Healthcare Life

141 Sciences) equipped with high-efficiency fluorochrome specific filter sets for DAPI, cy3 and cy5

142 (11) . For multiplexed staining where co-localization was desired, the regions of interest (~0.4–

143 0.6 mm^2 tissue area) were imaged, and stage coordinates were saved. The coordinates of each

144 image region were then recalled for each subsequent round after minor readjustment using

145 reference points from the first-round DAPI image and determining the appropriate offset. The

146 exposure times were set at a fixed value for all images of a given marker. For image analyses,

147   microscopy images were exported as full- resolution TIFF images in grayscale for each

148   individual channel collected.

149   <u>MultiOmyx image analytics.</u> The acquired images from sequential rounds were registered using

150   DAPI images acquired in the first round of staining via a rigid registration algorithm for each

151   region of interest. The parameters of transformation were then applied to the subsequent

152   rounds, which ensured that the pixel coordinates across all the imaging rounds corresponded to

153   the same physical locations on the tissue. Classification and co-expression analysis were

154   performed in multiple stages. First, a nuclear segmentation algorithm was applied on the DAPI

155   image to delineate and identify individual cells. Location information and expression of all the

156   markers were computed for every cell identified. Then, morphologic image analysis and shape

157   detection were performed using proprietary algorithms. These algorithms detect and classify

158   cells as positive or negative for each marker depending on their subcellular localization and

159   morphology. A tissue-quality algorithm was also applied to the images to ensure image artifacts

160   that arose owing to tissue folding or tear did not affect cell classification. Co-expression analysis

161   and phenotype identification were performed by combining individual marker classification

162   results.

163   <u>αSMA Morphology.</u> The αSMA morphology of 3 ROIs per tumor were independently scored by

164   2 investigators (NKA and TEM) as either organized (value of 1) or disorganized (value of 0).

165   Representative images of these 2 classes of morphology are shown in Figure 9. Each tumor

166   was assigned a predominant αSMA morphology based on the sum score: disorganized ≤ 1;

167   organized ≥ 2.

168   <u>Statistical Analysis</u>**.** Students unpaired T tests or Fishers exact test, where appropriate, were

169   used to evaluate group differences (Prism, GraphPad Software). All reported p values are

170   significant based on Benjamini-Hochberg control for false discovery at an alpha of 0.05.

RESULTS

Defining the tumor microenvironment by multiplex immunofluorescence analyses

We used multiplex immunofluorescence microscopy to contrast the TME of both pure non-solid CT scan density (p-NS) and solid early stage human LUADs. We generated a tissue microarray (TMA) of stage 1A LUADs: 25 p-NS tumors and 27 solid tumors (supplemental Table I). To capture the heterogeneity within individual tumors the TMA was constructed from different cores (regions of interests, ROI's) of each tumor. The expressions of all markers were determined in at least 3 ROIs per tumor and some markers were measured in 6 ROIs per tumor. A TMA of normal lung was generated from tissue adjacent to the tumors of 49 subjects (a single core per sample). The Neogenomics multiplex immunofluorescence platform (11) was used to quantify expressions of 19 markers to define the immune cell composition and activation states, to identify cancer/epithelial cells and fibroblasts (Fig. 1A and supplementalTable II). Briefly, the TMAs are stained with two different antibodies directly labeled with either Cy3 or Cy5 fluorophores. Images in both channels are collected, the Cy3 and Cy5 fluorescence inactivated, samples washed, stained with 2 new antibodies directly labeled with Cy3 or Cy5, images collected and the process repeated (12). In this iterative fashion the TMAs were stained with 20 antibodies. A representative multiplexed image is shown in figure 1B.

The CT density-defined groups were matched for age, sex and tumor size (supplemental Table I). In the p-NS group there were equal numbers of EGF receptor (EGFR) mutant and KRAS tumors (28% each), whereas in the solid group there were 3 times as many KRAS (37%) as mutant EGFR tumors (11%). Within the constraints of our sample size, we were unable to detect a significant differences in the immune compositions of KRAS and mutant EGFR TMEs, either within a tumor group or between the two tumor groups. Tumors in the CT solid group were significantly more invasive than the p-NS tumors (Fig. 1C), supporting the use of CT density as a means to classify tumors for analyses of how the TME changes with tumor progression. The percentage of Ki67$^+$ panCK cells in the solid tumor group was significantly increased relative to the p-NS, confirming that the CT dense tumors are more proliferative (Fig. 1D).

p-NS and solid tumors are equally T cell inflamed compared to normal lung

T cell density (CD3$^+$ cells) was significantly elevated in both the p-NS and solid tumor groups compared to the normal lung group, whereas there was no significant difference in T cell density between p-NS and solid tumor groups (Fig. 1E). Therefore, neither the emergence of a p-NS tumor from normal lung nor the progression from p-NS to solid tumors are characterized by

204   exclusion of T cells from the tumor mass. In addition, intra-tumor heterogeneity in T cell

205   densities, assessed by the coefficient of variation of T cell density among the 6 ROIs per tumor,

206   were similar in the two tumor groups, establishing that intra-tumor heterogeneity in T cell density

207   does not change significantly during progression of p-NS to solid tumors (Fig. 1F).

208   To broadly define the TME of the groups, we also determined the density of B cells (CD3$^-$CD19$^+$

209   cells), macrophages (CD3$^-$ CD68$^+$ CD209$^-$ cells), dendritic cells (CD3$^-$ CD209$^+$ CD68$^-$ cells) and

210   fibroblasts (CD3$^-$ panCK$^-$ αSMA$^+$ cells). Alpha smooth muscle actin (αSMA) is frequently used as

211   a marker of cancer-associated fibroblasts, although it is expressed in other cell types, most

212   prominently myofibroblasts and pericytes (13). Here we refer to αSMA$^+$ cells as fibroblasts. B

213   cell density in the normal lung was low (0.06% of total cells) and significantly elevated in both p-

214   NS and solid tumor groups (2.7% and 2.1% of total cells, respectively) (Fig. 1G). However, there

215   was no significant difference in B cell density between the two tumor groups. There was a small

216   yet significant reduction in macrophage cell density in the solid tumor groups compared to

217   normal lung, whereas there was no difference between the p-NS group and the normal lung

218   (Fig. 1H). Neither the dendritic cell density nor fibroblast cell density varied significantly among

219   the three groups (Fig. 1I & J).

220   The TMEs of p-NS tumors are enriched for Treg cells

221   We investigated the T cell subtype compositions to determine whether the TME of p-NS tumors

222   were predominantly immune-suppressive. CD4$^+$ T cells (CD3$^+$CD4$^+$) were significantly

223   increased in the p-NS tumor group (Fig. 2A). The subtype composition of the CD4$^+$ T cells also

224   varied between the normal lung and p-NS tumor groups. Immune-suppressive Treg cells (CD3$^+$

225   CD4$^+$ FoxP3$^+$ cells) were significantly increased in the p-NS tumor group at the expense of T

226   helper cells (CD3$^+$ CD4$^+$ FoxP3$^-$ cells) and approximately 5% of the Treg cells in the p-NS group

227   were Ki67$^+$ (Fig. 2B&C). Importantly, CTLA-4$^+$ Treg cells were enriched in the p-NS tumor group

228   compared to normal lung, approximately 2% of which were Ki67$^+$ (Fig. 2D&E). CTLA-4

229   expression is associated with enhanced Treg activity and homeostasis (14,15). These data

230   demonstrate an increased immune-suppressive TME in p-NS tumor group compared to normal

231   lung.

232   The density of cytotoxic T (CD3$^+$CD8$^+$) cells, as the proportion of T cells, did not differ between

233   normal lung and p-NS tumor groups (Fig. 2F). However, granzyme B (GZB) expressing

234   cytotoxic cells (GZB$^+$CD8$^+$CD3$^+$ cells) were reduced in the p-NS tumor group relative to normal

235   lung (Fig. 2G). GZB expression distinguishes active from resting or memory cytotoxic T cells. In

236   addition, less than 1% of the active cytotoxic T cells in the p-NS tumor group were positive for

237   the proliferation marker Ki67 (Fig. 2H). The ratio of Treg cells to cytotoxic T cells per individual

238   sample was significantly elevated in the p-NS group that the normal lung group (Fig. 2I),

239   supporting the hypothesis that in individual p-NS tumors both an increase in Tregs and a

240   decrease in CD8 T cells contribute to an immune-suppressive TME.

241   Expression of immune checkpoints is a mechanism by which tumors evade immune-mediated

242   killing (16). There was no difference between normal lung and p-NS tumor groups in two

243   immune checkpoints known to be upregulated in LUADs (13): PD-L1$^+$ or TIM-3$^+$ (Fig. 2J&K). In

244   addition, there was no difference in PD1$^+$ T cells, whose expression is often used as marker of T

245   cell exhaustion/dysfunction (17) (Fig. 2L). MHC class I$^+$ cell density (HLA-ABC$^+$) was elevated

246   in the p-NS tumors, demonstrating that reduced MHC class I antigen presentation is not a

247   mechanism for immune escape in p-NS tumors (Fig. 2M). There was no difference between

248   normal lung and p-NS tumor group in MHC class II expression (HLA-DR$^+$ cells) (Fig. 2N).

249   However, there was an increase in the p-NS tumor group of CD45RO$^+$ cells, a marker of

250   memory T cells, consistent with an increase in antigen-experienced cells in the p-NS tumors

251   (Fig. 2O).

252   Our analyses of the immune TME of p-NS tumors compared to adjacent normal lung support

253   the hypothesis that in the p-NS tumors, an early manifestation of LUAD, cancer cells evade

254   immune-mediated cell killing predominately through mechanisms involving a TME enriched with

255   immune-suppressive Treg cells and depleted for activated cytotoxic T cells.

256   Increased active Treg cells and cytotoxic T cells in the solid tumor group

257   We next compared the immune-TME of the p-NS and solid tumor groups by assessing the

258   composition and activation states of the T cells. There was no difference in CD3$^+$CD4$^+$ cell

259   density between p-NS and solid tumor groups, regardless of whether CD4$^+$ cells were analyzed

260   as the percent of total cells or as the percent of CD3$^+$ cells (Fig. 3A & B). In both tumor groups

261   about 70% of the T cells were CD4$^+$ cells. However, the proportions of CD4$^+$ cells that were

262   immune-suppressive Treg cells were significantly increased in the solid tumor group (Fig. 3C).

263   An equal proportion of Tregs were Ki67$^+$ in both groups (Fig. 3D). However, the proportion of

264   CTLA-4$^+$ Treg cells was significantly elevated in the solid tumor group, consistent with an

265   increased immune-suppressive TME of solid tumors relative to the p-NS tumors (Fig. 3E).

266   There was no significant difference in cytotoxic T cell (CD3$^+$CD8$^+$) density between the groups

267   when measured as a proportion of total cells (density in tissue) or as a proportion of CD3$^+$ cells

268   (Fig. 3F&G). There was, unexpectedly, an increase in activated cytotoxic T cells

269   (CD3$^+$CD8$^+$GZB$^+$) as well as Ki67$^+$ active CD8 cells in the solid tumor group (Fig. 3H&I). Thus,

270   there is an active cytotoxic immune response in the more advanced solid tumors. The

271   corresponding increase in immune-suppressive Treg cells may serve to counter-balance the

272   increase in cytotoxic cells, thereby contributing to a blunting of activated cytotoxic T cells.

273   Supporting that hypothesis, there was a positive correlation between the densities of Treg cells

274   and GZB$^+$CD8 cells in the solid tumor group (Fig. 3J).

275   We explored other potential immune-suppressive mechanism to account for the suppression of

276   cytotoxic T cell response in the solid tumor group. There were no differences between the p-NS

277   and solid tumor groups in PD1$^+$ checkpoint expression in cytotoxic T cells (PD1$^+$CD8$^+$) (Fig. 4A).

278   Hence, cytotoxic T cell "exhaustion" does not underlie immune suppression of the TME in solid

279   tumors. There was, however, an increase in PD1$^+$ Thelper cells (PD1$^+$CD3$^+$CD4$^+$FoxP3$^-$),

280   indicating potential checkpoint-mediated blunting of T helper function contributing to the immune

281   suppressive TME of solid tumors (Fig. 4B). There was no difference in expression of the TIM3$^+$

282   checkpoint between the groups (Fig. 4C).

283   The densities of MHC class I-expressing cells (HLA-ABC$^+$) were not different between the two

284   tumor groups, demonstrating that in the more advanced solid tumors, cancer cells do not evade

285   immune surveillance by reduced MHC class I antigen presentation (Fig. 4D). There were no

286   differences in MHC class II expressing macrophages (HLA-DR$^+$CD68$^+$CD3$^-$CD209$^-$) nor

287   dendritic cells (HLA-DR$^+$ CD209$^+$CD3$^-$CD68$^-$) between the groups (Fig. 4E&F).

288   Upregulation of the tryptophan catabolic enzyme, indoleamine 2,3-dioxyhydrogenase (IDO), can

289   have an immune suppressive role in cancer (16). Because IDO can be expressed by either

290   cancer cells or cells of the tumor stroma, we compared the p-NS and solid tumor groups for total

291   IDO expressing cells (Fig. 4G). There was no difference in IDO expression between the tumor

292   groups, although two solid tumors expressed IDO at a higher frequency than the others.

293   Although IDO expression might have an immune suppressive role in these two solid tumors,

294   increased IDO expression does not underlie enhanced immune suppression in the solid tumor

295   group compared to the p-NS tumor group (inset Fig. 4G).

10

296   Arginase 1, expressed by cells of the TME, has an inhibitory effect on antigen-specific anti-

297   tumor T cell responses (18). As was the case for IDO, Arginase expression does not distinguish

298   the tumor groups, therefore Arginase I upregulation is not a common immune-suppressive

299   mechanism in the solid tumor group (Fig. 4H). The frequency of arginase expression is

300   elevated in 2 of the solid tumors (not the same as those in which IDO is upregulated),

301   suggesting elevated Arginase might in some tumors have an immune suppressive role.

302   Heterogenous expression of PD-L1 among the solid tumor group

303   Expression of the PD-L1 checkpoint is a mechanism for immune escape in NSCLC and the

304   percent of cancer cells expressing PD-L1 is used clinically to assess overall PD-L1 expression

305   in tumors (19). In the p-NS tumor group only 3 of 25 tumors had greater than 1% PD-L1$^+$ panCK

306   cells, whereas in the solid tumor group 13 of 29 had greater than 1% PD-L1+ panCK cells (Fig.

307   5A&B). Because of the broad range of PD-L1 expression among the solid tumors, we

308   segregated them into three groups: tumors with less than 1% PD-L1$^+$ panCK cells; tumors with

309   less than 50% PD-L1$^+$ panCK cells; tumors with greater than 50% PD-L1$^+$ panCK cells. Total

310   tumor-mass infiltrating T cells did not correlate with PD-L1 expression but higher PD-L1

311   expression in panCK cells correlated with an increase in activated cytotoxic T cells

312   (CD3$^+$CD8$^+$GZB$^+$) and CTLA-4$^+$Tregs (CD3$^+$CD4$^+$FoxP3$^+$) (Fig. 5C-E). No differences in the

313   immune profiles of the low and intermediate PD-L1 expressing tumor groups were detected.

314   Thus, a high percentage of PD-L1 expressing panCK$^+$ cells was linked to increases in both

315   immune suppressive and cytotoxic T cells. These data support the hypothesis that an anti-

316   cancer cytotoxic T cell immune response was blunted by both the immune suppressive activities

317   of Treg cells and an increase PD-L1 expression.

318   There was a positive correlation between PD-L1 expression in panCK$^+$ cells and PD-L1

319   expression in T cells as well as fibroblasts within the same tumors (Fig. 5F). Thus, upregulation

320   of PD-L1 is not restricted to cancer cells (panCK$^+$ cells) but rather enhanced PD-L1 expression

321   reflects conditions within the TME.

322   Expression of PD1 was increased in cytotoxic T cells of the high PD-L1 expressing tumor group

323   (Fig. 5G). PD1 expression was increased in T helper cells of tumors in the highest PD-L1

324   expressing group compared to the intermediate and no PD-L1 expressing tumor groups (Fig.

325   5H). There were no differences among the groups in PD1$^+$ Tregs (Fig. 5I). PD1, a negative

326   feedback receptor, is expressed on both activated and "exhausted" T cells, and therefore its

327   expression alone does not establish the activated state of T cells. However, high PD1

11

328   expression in an environment of high PD-L1 expression indicates active checkpoint function.

329   Consequently, in the high PD-L1 expressing tumor group, both the anti-tumor T helper and

330   cytotoxic T cells are likely to be suppressed, relative to the lower PD-L1 expressing tumor

331   groups.

332   T Cell exclusion from cancer cell nests as an immune-suppressive mechanism in p-NS tumors

333   The spatial distribution of T cells within the tumor mass, either localized to the stroma or

334   infiltrated among the cancer cells nests, impacts immune response to the cancer cells since the

335   physical proximity of T cells to cancer cells is required for cytotoxic T cell function. Restriction of

336   intra-tumoral T cells to the stroma (fibroblast-rich) and exclusion from the parenchyma is a

337   mechanism for evasion of immune surveillance (2,5,20,21).

338   We quantified the spatial distribution of T cells within the stroma or cancer cell nests based on a

339   panCK$^+$ mask. A frequency distribution histogram based on T cell infiltration of cancer cell beds

340   (percent total tumor T cells) revealed increased T cell infiltration in the solid tumor group (Fig.

341   6A). To explore differences in the immune composition based on localization within the tumor

342   (that is, stroma or cancer cell nests), we used a value of greater than or equal to 5% of T cells

343   (CD3$^+$) within cancer cells nest to segregate tumors into 'high' and 'low' T cell infiltration of

344   cancer cell nests (Fig. 6A). There was a trend towards increased infiltration of T cells among the

345   cancer cell nests in the solid tumor group: 74% of the solid tumors and 52% of the p-NS had

346   high T cell infiltration of the cancer cell nests (p=0.15, Fischer's Exact Test). However,

347   differences in the compositions of the T cells within the cancer cells nests between the two

348   tumor groups were similar to those differences in the tumor not segregated for location, with an

349   increase of both Treg cells and cytotoxic cells in the solid tumor group (Fig. 6B&C).

350   T cell infiltration into the cancer cell nest of the solid tumors was highest in those tumors with

351   the highest PD-L1 expression, in line with induced PD-L1 expression protecting the cancer cells

352   from the cytotoxic T cells that had invaded the cancer cell nest (Fig. 6D). There were no

353   differences in total tumor-mass infiltrating T cells between the p-NS and solid tumor groups (Fig.

354   1E). Therefore, exclusion of the T cells from the cancer cell nests, rather than from the tumor

355   mass per se, is potentially a more important mechanism for immune escape in the p-NS tumor

356   group than it may be in the solid tumor group.

357   Fibroblasts morphology varies between the p-NS and solid tumors groups

358   Staining for alpha smooth muscle actin (αSMA) as a marker of fibroblasts revealed two

359   prominent morphologies represented in both tumor groups. In one, the αSMA was well

360   organized, circumscribing the cancer cell nests (panCK$^+$) (Fig. 7A&B). In the other the αSMA

361   pattern was disorganized and fragmented (Fig. 7C&D). The disorganized fibroblasts structure

362   (αSMA morphology) was significantly more prevalent in the solid tumors (Fig. 7E). These data

363   associate a disorganized αSMA morphology with the more advanced tumor group.

364   Furthermore, in the p-NS tumor group the degree of T cell infiltration among the cancer cells

365   was significantly decreased in tumor areas (ROIs) of organized αSMA morphology, correlating

366   the intact fibroblastic structure with reduced accumulation of T cell among the cancer cells, a

367   correlation not observed in the solid tumors (Fig. 7F).

DISCUSSION

Immune escape is essential for tumor progression, and a more thorough understanding of the cellular and molecular mechanism(s) by which preinvasive malignancies escape immune surveillance may allow for the development of more effective interception strategies that can be deployed at the earliest manifestations of disease (20-22). Currently there are significant gaps in our understanding of the molecular and cellular events driving immune escape in preinvasive lung lesions. Although there have been recent reports on the genomic and transcriptomic landscapes of preinvasive squamous cell cancer (23,24) there are only a few studies of pre-invasive pulmonary adenocarcinoma, and even fewer that focused on the immune milieu in tumor microenvironment. The most comprehensive profiling of the TME, reported by Lavin *et al*, was focused on clinically evident early lung cancers rather than precursor lesions (25). A more recent report by Chen et al, reported on 98 precursor lesions of lung adenocarcinoma and found that immune infiltration is correlated with copy number alterations of chromosome arm 6p suggesting a link between arm-level events and the tumor immune environment (26). Our limited understanding of the early events associated with progression of precursor lesions of LUAD is at least partly due to the difficulty in accessing sufficient material from these small lesions in humans for study. Typically, LUAD precursor lesions are situated peripherally in the lung parenchyma where they are inaccessible by bronchoscopic approaches and therefore tissue sampling is only possible after surgical removal. In this study we contrasted two extremes on the radiographic spectrum, the pure non-solid nodule which generally (but not always) harbors pre or minimally invasive adenocarcinoma and the solid nodule representing frankly invasive cancers. The choice of extremes was designed to allow us to maximize and capture significant molecular events associated with transition to a more invasive phenotype.

Evolution of preinvasive adenocarcinoma in pure non-solid tumors

We found that compared to adjacent normal lung, the stroma of p-NS tumors was intensely infiltrated by immune cells, an infiltration predominantly composed of $CD3^+$ T cells. The composition of the $CD3^+$ population was dominated by $CD4^+$ cells that accounted for nearly two thirds of all T cells within the tumor nodule. Significantly, immune-suppressive regulatory T cells ($CD3^+CD4^+FoxP3^+$) were twice as prevalent in the p-NS tumor group than in normal lung (Fig. 2). Approximately 10% of the Tregs in p-NS group expressed the activation marker CTLA-4, whereas less than 1% of Tregs in normal lung were CTLA-4$^+$ (Fig. 2). Although, the proportion of cytotoxic T cells ($CD3^+CD8^+$) in the p-NS tumor nodule group was essentially the same as in normal lung, the proportion of $GZB^+ CD8^+$ T cells was almost three-fold lower than that in normal

401   lung and nearly all lacked Ki67 expression, suggesting a possible exhausted phenotype (Fig. 2).

402   On a per tumor basis, the Treg cell-to-CD8$^+$ cell ratio was significantly higher in the tumor

403   nodule than in normal lung, indicating the dominance of Treg-mediated immunosuppressive

404   effect. We also found that the expression of MHC class I molecules and CD45RO$^+$ cells were

405   significantly higher in tumor nodules than in normal lung, demonstrating that escape from

406   immune surveillance was not mediated by aberration in antigen presentation (Fig. 2).

407   Interestingly, expression of the inhibitory checkpoints PD1, PD-L1 and Tim-3, were not

408   upregulated in the p-NS tumor group, suggesting that immune privilege of p-NS nodules does

409   not result from activation of inhibitory immune checkpoints.

410   Evolution of early solid invasive adenocarcinoma

411   We made several observations when comparing the immune TME profile of lung

412   adenocarcinoma presenting as a solid tumor with that arising in p-NS nodules. Our findings

413   strongly support the hypothesis that multiple modes of tumor escape develop during transition to

414   an invasive phenotype. First, although adenocarcinomas arising in both types of nodules were

415   equally T cell inflamed (Fig. 1), those in solid nodules had a significantly higher proportion of

416   regulatory T cells, with a two-fold increase in the proportion of immune suppressive Treg cells

417   (CD3$^+$CD4$^+$FoxP3$^+$) that expressed CTLA-4 (Fig. 3). There was also an associated three-fold

418   increase in the number of activated cytotoxic T cells (GZB$^+$CD8$^+$) cells in the solid tumors (Fig.

419   3), suggesting a nascent albeit ineffective anti-tumor immune response. It is likely that any

420   emergent anti-tumor immune response may have been at least partially restrained by Treg cell-

421   mediated immune suppression. In the context of the immune editing hypothesis for tumor

422   progression, these data indicate that the transition from p-NS to solid nodules reflects a shift

423   from equilibrium to escape phase of immune editing (9). Second, while there was essentially no

424   PD-L1$^+$ expression in panCK$^+$ cells of the p-NS group, collectively solid nodules had a

425   significantly higher frequency of PD-L1$^+$panCK$^+$ cells (Fig. 5). Thus, expression of the PD-L1

426   inhibitory immune checkpoint, an established mode of immune evasion potentially deployed by

427   cancer cells possibly due to the release of interferon gamma from activated cytotoxic T cells,

428   was only observed in more advance tumors.

429   PD-L1 expression defines two immune phenotypes of solid adenocarcinoma

430   PD-L1 expression in panCK$^+$ adenocarcinoma presenting as a solid nodule identified three

431   distinct sub-groups based on the frequency of PD-L1 expression. Tumors in which 50% or more

432   of the panCK$^+$ cells expressed PD-L1, a threshold commonly used in the clinic for treating stage

433   IV lung cancer patients with anti-PD-1 alone (that is, without chemotherapy), were grouped as

434   high PD-L1 expressers. Tumors in which greater than 1% but less than 50% of the panCK$^+$

435   were PD-L1$^+$ were classified as a separate group as were those in which PD-L1 expression in

436   panCK$^+$ was less than 1%. Tumors with high PDL-1 expression in panCK$^+$ cells were associated

437   with higher PD-L1 expression in various T cell subsets and fibroblasts. High expressers had a

438   distinctive immune phenotype characterized by more intense T cell infiltration, and broad

439   activation of the adaptive immune response, including significantly higher frequencies of PD1$^+$

440   cytotoxic T cells (CD3$^+$CD8$^+$GZB$^+$) and PD1$^+$ cytotoxic T helper cells (CD3$^+$CD4$^+$ FoxP3$^-$) and

441   CTLA-4$^+$ Treg cells (CD3$^+$CD4$^+$ FoxP3$^+$). This defines tumors that are most likely to respond to

442   dual immune check point inhibition targeting CTLA-4 and/or the PD1/PDL-1 axis. There was no

443   significant difference in either the composition or activation state of immune cells of the TME

444   between low and intermediate expressers of PD-L1, which might reflect a relatively quiescent

445   immune response. In this group of patients, response to immune checkpoint inhibition alone

446   may be unlikely and this is reflected to some extent in clinical practice where such patients are

447   treated by a combination of chemotherapy and immune checkpoint inhibition (27).

448   T cell infiltration into the cancer cell nests is also immune-suppressive

449   The phenomenon of T cell exclusion has been previously reported as a mechanism of immune

450   evasion in multiple cancers including pancreatic, ovarian and colorectal cancer (28-30). A

451   similar finding was observed in ductal carcinoma *in-situ* breast cancer where cancer cells are

452   separated from tumor infiltrating T cells by a continuous layer of myoepithelial cells and

453   myofibroblasts (31). T cell exclusion from the entire tumor mass was not observed in any of our

454   cases. However, T cell exclusion from the cancer cell nests was observed in nearly 50% of all

455   tumor nodules classified radiographically as p-NS and in 25% of solid nodules that represented

456   frankly invasive adenocarcinoma. In all remaining cases there was infiltration of CD3$^+$ T cells

457   into the cancer cell nests where they were interspersed with the cancer cells. The immune

458   phenotype of the T cells in the cancer cell nests mirrored that of CD3$^+$ T cells in the stroma and

459   was dominantly immune suppressive.

460   Fibroblastic architecture possibly associated with T cell exclusion

461   To investigate whether fibroblastic spatial organization is associated with T cell exclusion we

462   scored each tumor for continuity of αSMA staining. The fibroblastic barrier appeared continuous

463   in 26% of all solid tumor nodules and interrupted or discontinuous in the remaining 74%. In the

464   latter cases the CD3 cells were predominantly interspersed among the cancer cells. In contrast,

465   in p-NS tumors the barrier was continuous in three quarters of patients and discontinuous in the

466   remainder. We found that a continuous fibroblastic barrier was significantly associated with T

467   cell exclusion in p-NS tumor group but not in the solid nodule group, probably because the

468   majority of solid nodules had a discontinuous barrier. Whether T cell exclusion in our samples

469   was the result of a mere physical structural separation or alternatively mediated by specific

470   chemokine/receptor signaling or both remains to be elucidated. Fearon and co-workers have

471   shown that ligation of CXCL12 expressed on cancer associated fibroblasts to its receptor

472   CXCR4 on cancer cells may contribute to T cell exclusion in pancreatic adenocarcinoma (32).

473   In summary, our data suggest a complex dynamic interaction between the tumor and its

474   immune microenvironment (Fig. 7G). A dominant regulatory T cell-mediated immune

475   suppression is initiated at the precursor level and is sustained with rising intensity throughout

476   malignant progression. T cell exclusion from the cancer cell nests appears to be an additional

477   mechanism of immune evasion deployed by some early invasive lung cancers, possibly until

478   tumor evolution leads to a durable, viable invasive phenotype that breaks down the fibroblastic

479   barrier. Throughout the entire process a nascent effector immune response is present but is

480   effectively thwarted by the immune-suppressive elements. These data suggest that different

481   interception strategies should be employed at different stages of tumor evolution.

489   **Author disclosures**: NKA has equity in Angiocrine Bioscience, TMRW, and View Point

490   Medical. OE is supported by Janssen and Eli Lilly research grants. He is scientific advisor and

491   equity holder in Freenome, Owkin, Volastra Therapeutics and One Three Biotech. TEM receives

492   research funding from Pfizer, Inc for unrelated studies. VM and ACB have nothing to disclose.

493

494   **Author contributions:**

495   **NKA:** conceptualized the project, contributed to experimental design, performed analysis and

496   interpretations, and wrote the manuscript.

497   **ACB:** contributed to experimental design, data analyses, and edited the manuscript.

498   **VM:** contributed to experimental design and edited the manuscript.

499   **OE:** contributed to experimental design, data analyses, and edited the manuscript.

500   **TEM:** conceptualized the project, contributed to experimental design, performed analysis and

501   interpretation, and wrote the manuscript.

References

1.   Kobayashi Y, Mitsudomi T. Management of ground-glass opacities: should all pulmonary lesions with ground-glass opacity be surgically resected? Transl Lung Cancer Res **2013**;2(5):354-63 doi 10.3978/j.issn.2218-6751.2013.09.03.

2.   Klemm F, Joyce JA. Microenvironmental regulation of therapeutic response in cancer. Trends Cell Biol **2015**;25(4):198-213 doi 10.1016/j.tcb.2014.11.006.

3.   Pyonteck SM, Akkari L, Schuhmacher AJ, Bowman RL, Sevenich L, Quail DF, *et al.* CSF-1R inhibition alters macrophage polarization and blocks glioma progression. Nat Med **2013**;19(10):1264-72 doi 10.1038/nm.3337.

4.   Turley SJ, Cremasco V, Astarita JL. Immunological hallmarks of stromal cells in the tumour microenvironment. Nat Rev Immunol **2015**;15(11):669-82 doi 10.1038/nri3902.

5.   Joyce JA, Fearon DT. T cell exclusion, immune privilege, and the tumor microenvironment. Science **2015**;348(6230):74-80 doi 10.1126/science.aaa6204.

6.   Ribatti D. The concept of immune surveillance against tumors. The first theories. Oncotarget **2017**;8(4):7175-80 doi 10.18632/oncotarget.12739.

7.   Teng MW, Galon J, Fridman WH, Smyth MJ. From mice to humans: developments in cancer immunoediting. J Clin Invest **2015**;125(9):3338-46 doi 10.1172/JCI80004.

8.   Smyth MJ, Ngiow SF, Ribas A, Teng MW. Combination cancer immunotherapies tailored to the tumour microenvironment. Nat Rev Clin Oncol **2016**;13(3):143-58 doi 10.1038/nrclinonc.2015.209.

9.   Schreiber RD, Old LJ, Smyth MJ. Cancer immunoediting: integrating immunity's roles in cancer suppression and promotion. Science **2011**;331(6024):1565-70 doi 10.1126/science.1203486.

10.   Pedersen JH, Saghir Z, Wille MM, Thomsen LH, Skov BG, Ashraf H. Ground-Glass Opacity Lung Nodules in the Era of Lung Cancer CT Screening: Radiology, Pathology, and Clinical Management. Oncology (Williston Park) **2016**;30(3):266-74.

11.   Xu-Monette ZY, Xiao M, Au Q, Padmanabhan R, Xu B, Hoe N, *et al.* Immune Profiling and Quantitative Analysis Decipher the Clinical Role of Immune-Checkpoint Expression in the Tumor Immune Microenvironment of DLBCL. Cancer Immunol Res **2019**;7(4):644-57 doi 10.1158/2326-6066.CIR-18-0439.

12.   Gerdes MJ, Sevinsky CJ, Sood A, Adak S, Bello MO, Bordwell A, *et al.* Highly multiplexed single-cell analysis of formalin-fixed, paraffin-embedded cancer tissue. Proc Natl Acad Sci U S A **2013**;110(29):11982-7 doi 10.1073/pnas.1300136110.

13.   Yoshida GJ, Azuma A, Miura Y, Orimo A. Activated Fibroblast Program Orchestrates Tumor Initiation and Progression; Molecular Mechanisms and the Associated Therapeutic Strategies. Int J Mol Sci **2019**;20(9) doi 10.3390/ijms20092256.

14.   Pedros C, Canonigo-Balancio AJ, Kong KF, Altman A. Requirement of Treg-intrinsic CTLA4/PKCeta signaling pathway for suppressing tumor immunity. JCI Insight **2017**;2(23) doi 10.1172/jci.insight.95692.

15.   Tang AL, Teijaro JR, Njau MN, Chandran SS, Azimzadeh A, Nadler SG, *et al.* CTLA4 expression is an indicator and regulator of steady-state CD4+ FoxP3+ T cell homeostasis. J Immunol **2008**;181(3):1806-13 doi 10.4049/jimmunol.181.3.1806.

16.   Rao S, Gharib K, Han A. Cancer Immunosurveillance by T Cells. Int Rev Cell Mol Biol **2019**;342:149-73 doi 10.1016/bs.ircmb.2018.08.001.

17.   Thommen DS, Schumacher TN. T Cell Dysfunction in Cancer. Cancer Cell **2018**;33(4):547-62 doi 10.1016/j.ccell.2018.03.012.

18.   Lemos H, Huang L, Prendergast GC, Mellor AL. Immune control by amino acid catabolism during tumorigenesis and therapy. Nat Rev Cancer **2019**;19(3):162-75 doi 10.1038/s41568-019-0106-z.

19.   Brody R, Zhang Y, Ballas M, Siddiqui MK, Gupta P, Barker C, *et al.* PD-L1 expression in advanced NSCLC: Insights into risk stratification and treatment selection from a

systematic literature review. Lung Cancer **2017**;112:200-15 doi 10.1016/j.lungcan.2017.08.005.

20. Bonaventura P, Shekarian T, Alcazer V, Valladeau-Guilemond J, Valsesia-Wittmann S, Amigorena S*, et al.* Cold Tumors: A Therapeutic Challenge for Immunotherapy. Front Immunol **2019**;10:168 doi 10.3389/fimmu.2019.00168.

21. Di Modugno F, Colosi C, Trono P, Antonacci G, Ruocco G, Nistico P. 3D models in the new era of immune oncology: focus on T cells, CAF and ECM. J Exp Clin Cancer Res **2019**;38(1):117 doi 10.1186/s13046-019-1086-2.

22. Vinay DS, Ryan EP, Pawelec G, Talib WH, Stagg J, Elkord E*, et al.* Immune evasion in cancer: Mechanistic basis and therapeutic strategies. Semin Cancer Biol **2015**;35 Suppl:S185-S98 doi 10.1016/j.semcancer.2015.03.004.

23. Teixeira VH, Pipinikas CP, Pennycuick A, Lee-Six H, Chandrasekharan D, Beane J*, et al.* Deciphering the genomic, epigenomic, and transcriptomic landscapes of pre-invasive lung cancer lesions. Nat Med **2019**;25(3):517-25 doi 10.1038/s41591-018-0323-0.

24. Mascaux C, Angelova M, Vasaturo A, Beane J, Hijazi K, Anthoine G*, et al.* Immune evasion before tumour invasion in early lung squamous carcinogenesis. Nature **2019**;571(7766):570-5 doi 10.1038/s41586-019-1330-0.

25. Lavin Y, Kobayashi S, Leader A, Amir ED, Elefant N, Bigenwald C*, et al.* Innate Immune Landscape in Early Lung Adenocarcinoma by Paired Single-Cell Analyses. Cell **2017**;169(4):750-65 e17 doi 10.1016/j.cell.2017.04.014.

26. Chen H, Carrot-Zhang J, Zhao Y, Hu H, Freeman SS, Yu S*, et al.* Genomic and immune profiling of pre-invasive lung adenocarcinoma. Nat Commun **2019**;10(1):5472 doi 10.1038/s41467-019-13460-3.

27. Ghandili S, Bardenhagen J, Izbicki JR. Pancreatic Metastasis from Endometrial Carcinoma. J Gastrointest Surg **2019**;23(2):377-8 doi 10.1007/s11605-018-3934-3.

28. Tauriello DVF, Palomo-Ponce S, Stork D, Berenguer-Llergo A, Badia-Ramentol J, Iglesias M*, et al.* TGFbeta drives immune evasion in genetically reconstituted colon cancer metastasis. Nature **2018**;554(7693):538-43 doi 10.1038/nature25492.

29. Sanchez-Paulete AR, Teijeira A, Cueto FJ, Garasa S, Perez-Gracia JL, Sanchez-Arraez A*, et al.* Antigen cross-presentation and T-cell cross-priming in cancer immunology and immunotherapy. Ann Oncol **2017**;28(suppl_12):xii74 doi 10.1093/annonc/mdx727.

30. Beatty GL, Winograd R, Evans RA, Long KB, Luque SL, Lee JW*, et al.* Exclusion of T Cells From Pancreatic Carcinomas in Mice Is Regulated by Ly6C(low) F4/80(+) Extratumoral Macrophages. Gastroenterology **2015**;149(1):201-10 doi 10.1053/j.gastro.2015.04.010.

31. Gil Del Alcazar CR, Huh SJ, Ekram MB, Trinh A, Liu LL, Beca F*, et al.* Immune Escape in Breast Cancer During In Situ to Invasive Carcinoma Transition. Cancer Discov **2017**;7(10):1098-115 doi 10.1158/2159-8290.CD-17-0222.

32. Feig C, Jones JO, Kraman M, Wells RJ, Deonarine A, Chan DS*, et al.* Targeting CXCL12 from FAP-expressing carcinoma-associated fibroblasts synergizes with anti-PD-L1 immunotherapy in pancreatic cancer. Proc Natl Acad Sci U S A **2013**;110(50):20212-7 doi 10.1073/pnas.1320318110.
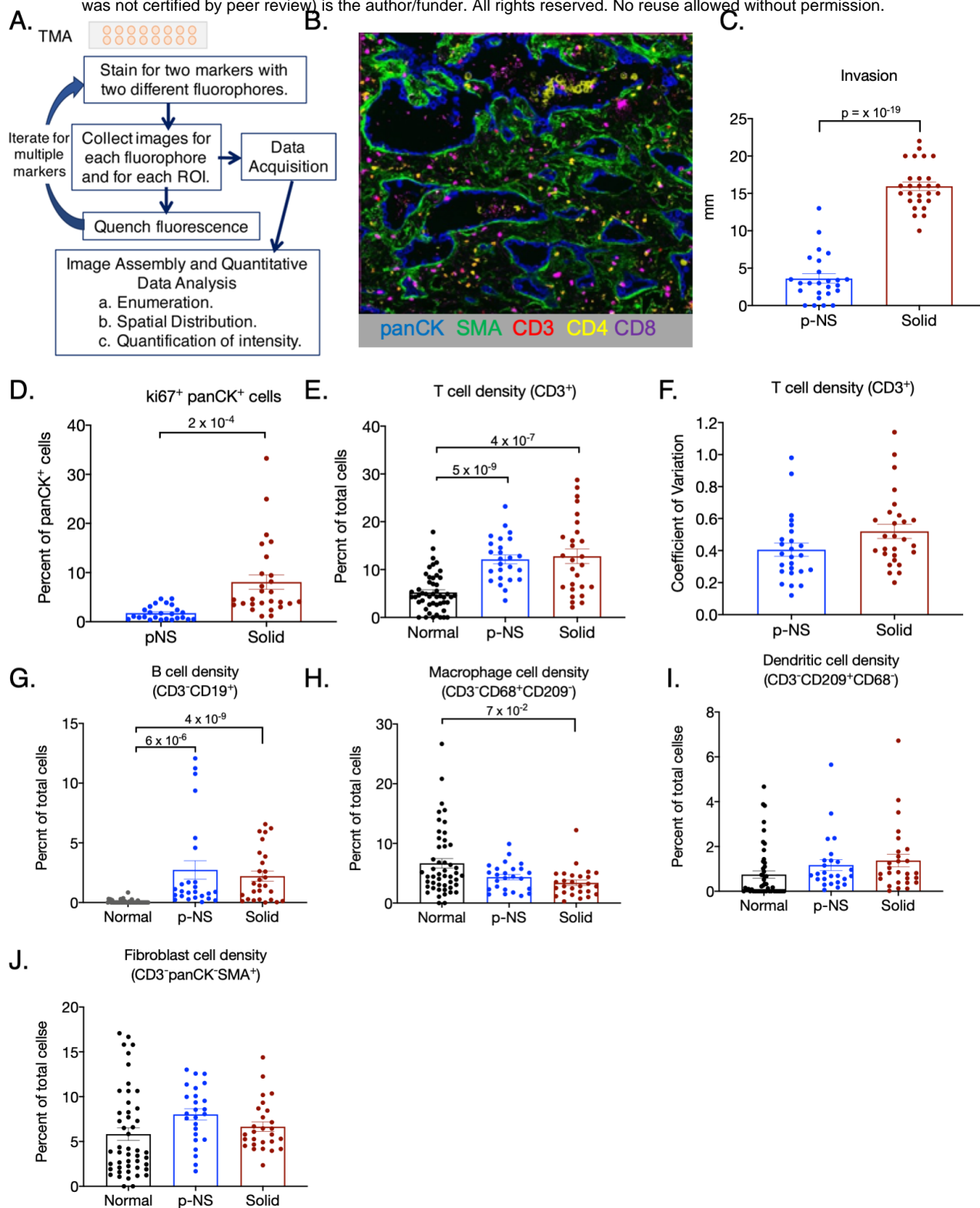
Figure 1. Immunofluorescence immune profiling. A. Cartoon of Neogenomics iterative, quantitative immunofluorescence platform. **B.** Representative Neogenomics pseudo-colored multiplex image, 200x magnification. Each channel scaled for purpose of presentation. **C.** Cancer cell invasion of the p-NS and solid tumor groups. **D.** Percent of panCK+ cells that are ki67+. **E.** Density of CD3+ cells determined as the percentage of total cells per ROI. **F** Coefficient of variations of CD3+ cell densities of the 6 ROIs per tumor of the p-NS and solid groups. **G.** Density of B cells (CD3-CD19+ cells) determined as the percentage of total cells per ROI. **H.** Density of macrophages (CD68+CD3- CD209- cells) determined as the percentage of total cells per ROI. **I.** Density of dendritic cells (CD209+CD3-CD68- cells determined as the percentage of total cells per ROI. **J.** Density of fibroblasts (CD3- panCK- SMA+) determined as the percentage of total cells per ROI. In all panels the symbols for normal tissue are data from a single ROI per sample, whereas in the p-NS and solid groups each symbol is the mean of 3 to 6 ROIs per tumor. Total cells were determined by DAPI stained nuclei per ROI. The group means ± SEM are shown. Statistically significant differences are noted. Student's t tests, unpaired. All p values shown are significant based on Benjamini-Hochberg control for false discovery at an alpha of 0.05.
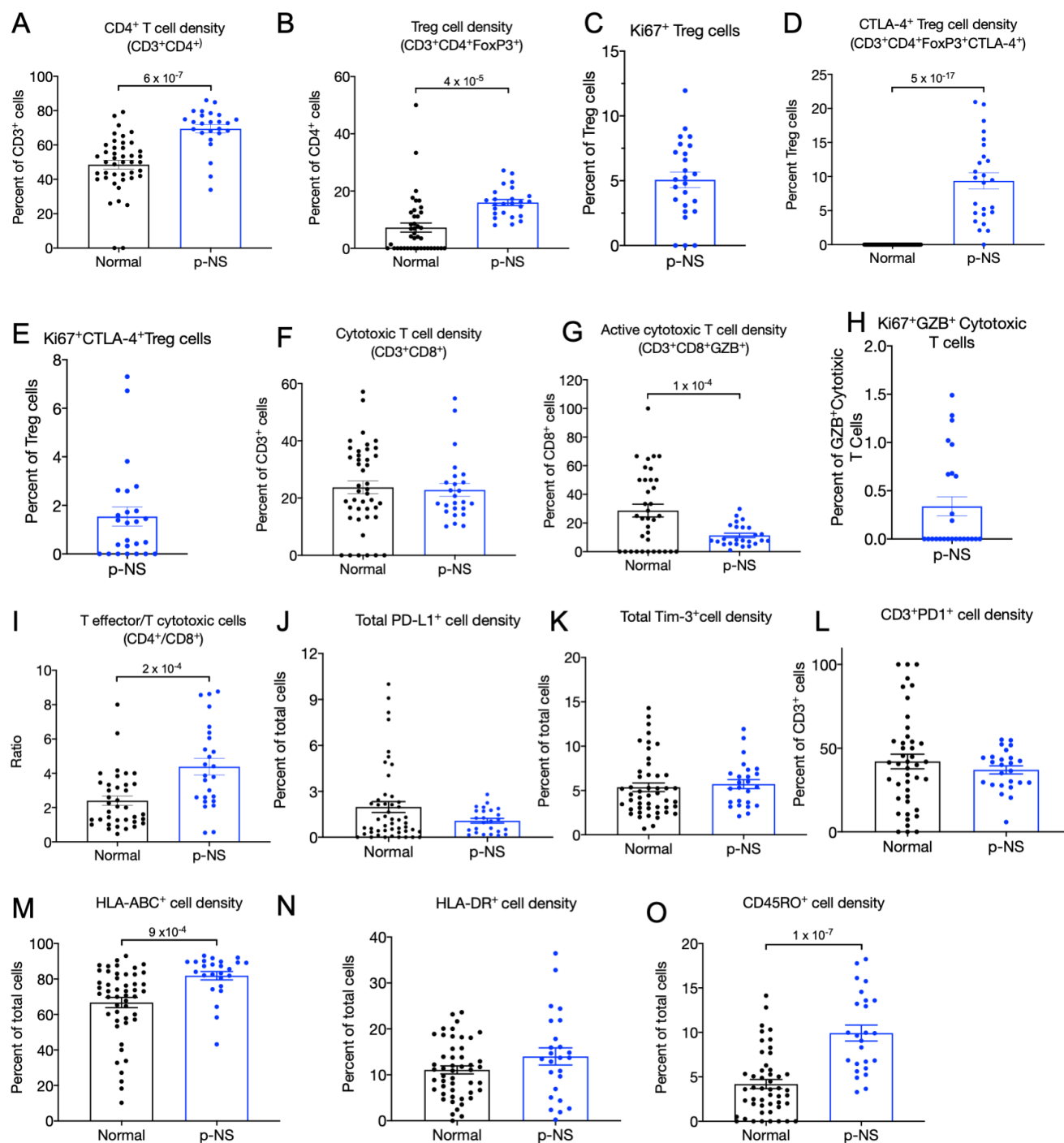
Figure 2. T cell composition. A. Densities of CD4+ cells determined as percentage of CD3+ cells. **B.** Treg cell densities (CD3+CD4+FoxP3+) determined as the percentage of CD3+CD4+ cells. **C.** Percent of Tregs in p-NS tumor group that are Ki67+. **D.** CTLA-4+ Treg cell densities (CD3+CD4+FoxP3+CTLA-4+) as the percentage of CD3+CD4+FoxP3+ cells. **E.** Percent of CTLA-4+ Tregs in p-NS tumor group that are Ki67+. **F.** Cytotoxic T cell densities (CD3+CD8+) determined as the percentage of CD3+ cells. **G.** Active cytotoxic T cells densities (CD3+CD8+GZB+) determined as the percentage of CD3+CD8+ cells. GZB, granzyme B. **H.** Percent of active cytotoxic T cells in p-NS tumor group that are Ki67+. **I.** Ratios per tumor of Treg cells (CD3+CD4+FoxP3+) to cytotoxic T cells (CD3+CD8+). **J.** Total PD-L1+ cell densities as a percentage of total cells. **K.** Total Tim-3+ cell densities determined as a percentage of total cells per ROI. **L.** Total PD1+ cells densities determined as a percentage of total cells per ROI. **M.** Total HLA-ABC+ cell densities determined as a percent of total cells per ROI. **N.** Total HLA-DR+ cell densities determined as a percentage of total cells per ROI. **O.** Total CD45RO+ cell densities determined as a percentage of total cells per ROI. In each comparison total cell numbers are defined by the number of DAPI stained nuclei per ROI. In all panels each normal tissue symbol is the cell density from a single ROI per sample, whereas in the p-NS group each symbol is the mean of 3 to 6 ROIs per tumor. The means ± SEM are shown for each group. Statistically significant differences are noted. Student's T test, unpaired. All p values shown are significant based on Benjamini-Hochberg control for false discovery at an alpha of 0.05.
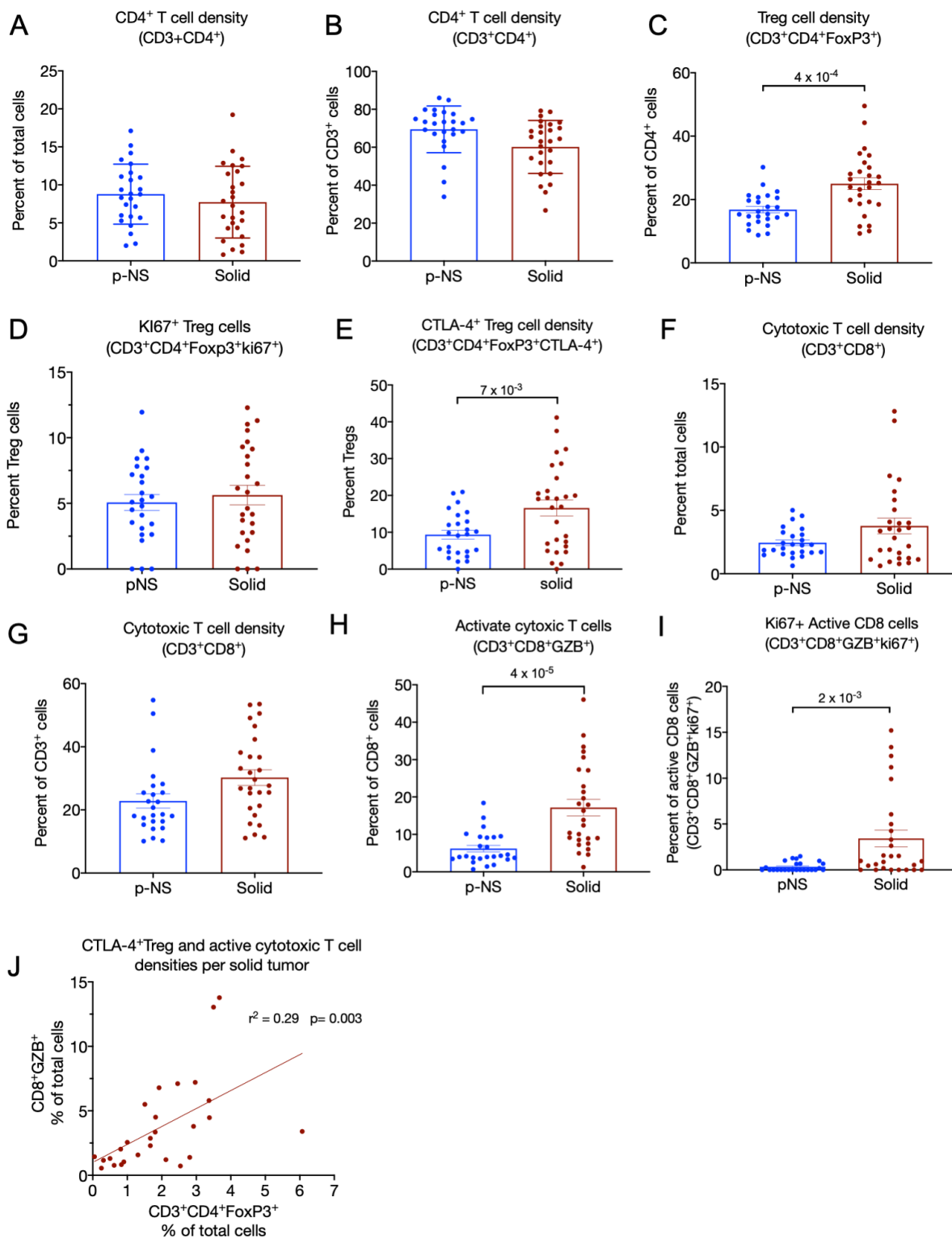
Figure 3. T cell compositions of p-NS and Solid tumors. A. CD4+ cell densities determined as a percentage of total cells per ROI. B. CD4+ cell densities determined as a percentage of CD3+ cells. C. Treg cell densities (CD3+CD4+FoxP3+) determined as a percentage of CD4+ cells. D. ki67+ Treg cell densities (CD3+CD4+FoxP3+ki67+) determined as a percentage of Treg cells. E. CTLA-4+ Treg cell densities (CD3+CD4+FoxP3+CTLA-4+) determined as a percentage of Treg cells. F. Cytotoxic T cell densities (CD3+CD8+) determined as a percentage of total cells per ROI. G. Cytotoxic T cell densities (CD3+CD8+) determined as a percentage of CD3+ cells. H. Active cytotoxic T cell densities (CD3+CD8+GZB+) determined as a percentage of CD3+CD8+ cells. GZB, granzyme B. I. ki67+ active CD8+ cell (CD3+CD8+GZB+ki67+) densities determined as a percentage of CD3+CD8+ cells. J. Correlation of CTLA-4+ Treg (CD3+CD4+FoxP3+CTLA-4+) and active cytotoxic T cell (CD3+CD8+GZB+) densities as percentages of total cells per ROI. The p value is for the difference in the slope of the correlation line from 0. In each panel the symbols are the means of 3 to 6 ROIs per tumor. The means ± SEM are shown for each group. Statistically significant differences are noted. Students T test, unpaired. All p values shown are significant based on Benjamini-Hochberg control for false discovery at an alpha of 0.05.
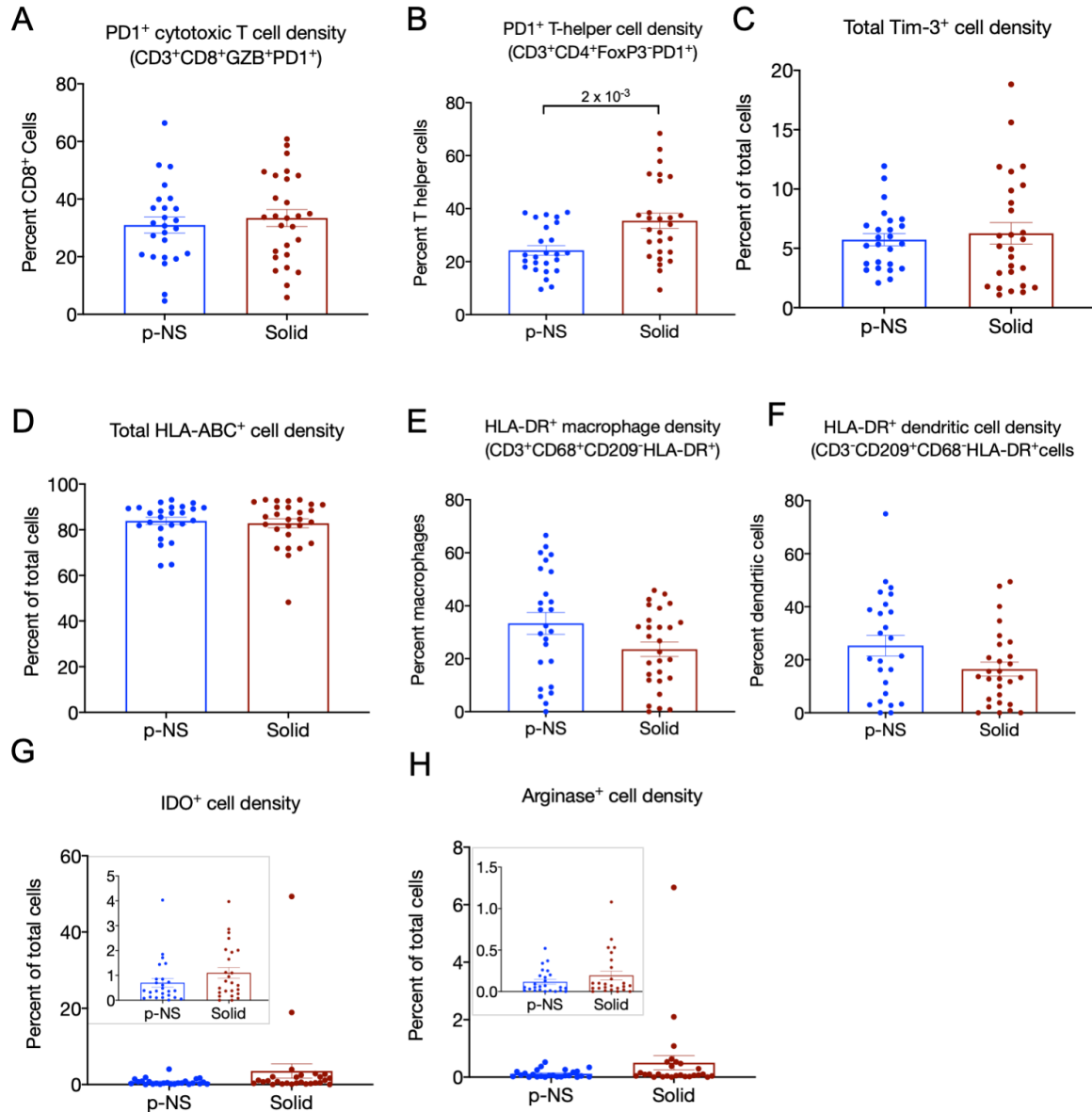
Figure 4. T cell activation states. **A.** PD1+ cytotoxic T cell densities determined as a percentage of CD8+ cells. **B.** PD1+ T helper cell (CD3+CD4+FoxP3-) densities determined as a percentage of T helper cells. **C.** Total TIM3+ cell densities. **D.** Total HLA-ABC+ cell densities determined as a percentage of total cells per ROI. **E.** HLA-DR+ macrophage densities determined as a percentage of total macrophages (CD3-CD68+CD209-). **F.** HLA-DR+ dendritic cell densities as percentage of dendritic cells (CD3-CD209+CD68-). **G.** IDO+ cell densities determined as a percentage of total cells. Inset, y axis expanded. **H.** Arginase+ cell densities determined as a percentage of total cells. Inset, y axis expanded. In all panels each symbol is the mean of 3 ROIs per tumor. The means ± SEM are shown for each group. Total cells determined by DAPI+ nuclei. Statistically significant differences are noted. Students T test, unpaired. All p values shown are significant based on Benjamini-Hochberg control for false discovery at an alpha of 0.05.
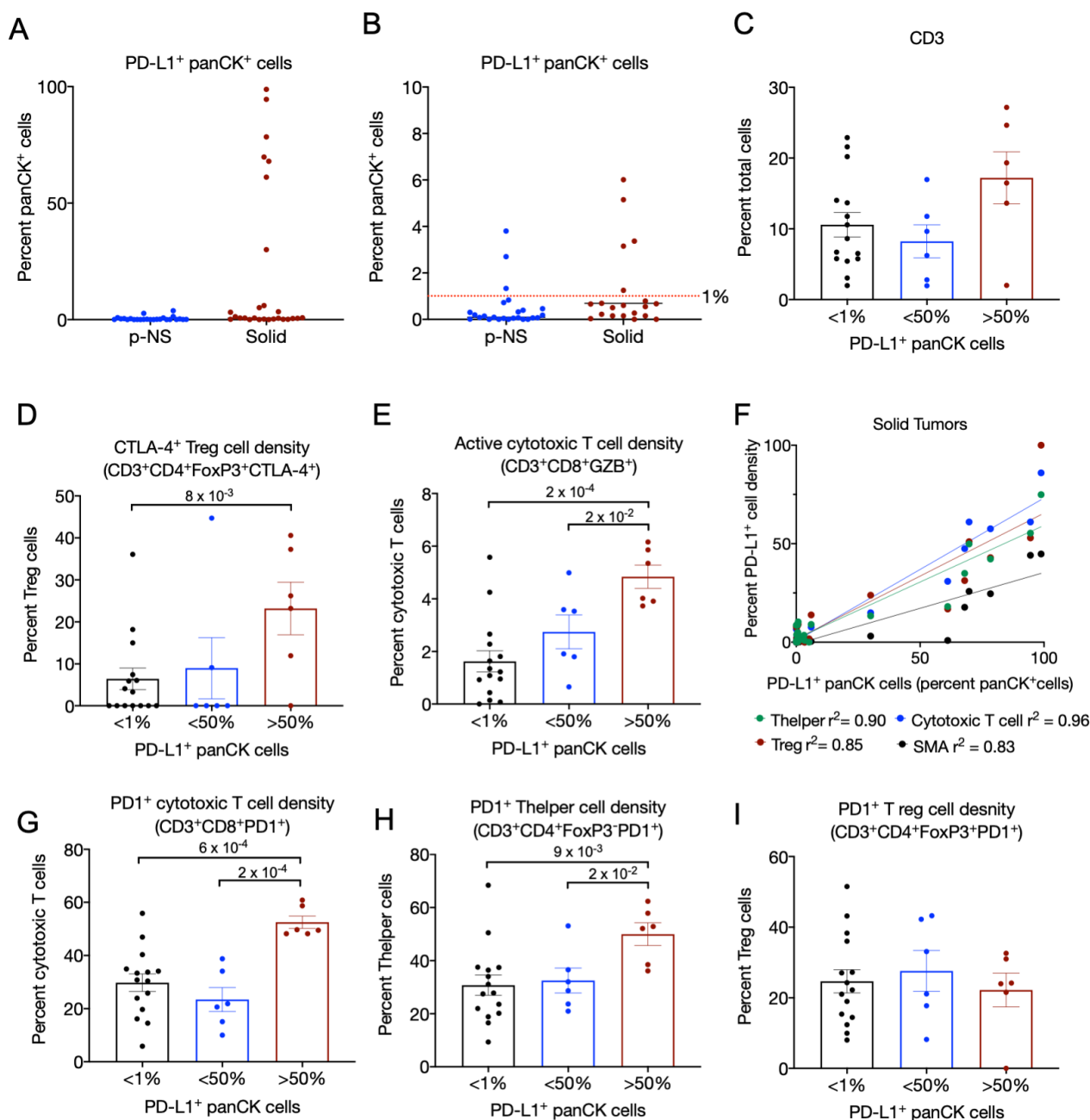
Figure 5. Immune profile linked to PD-L1 expression. A. PD-L1+panCK+ cells as a percentage of panCK+ cells. **B.** PD-L1+panCK+ cells, percent of panCK+ cells, on expanded y-axis to visualize differences among the low PD-L1 expressing tumors. The red dotted line is at 1% PD-L1+panCK cells. **C., D., & E.** Densities of CD3+ cells, CTLA-4+ Treg cells (CD3+CD4+FoxP3+CTLA-4+) and active cytotoxic T cells (CD3+CD8+GZB+) in the 3 subcategories of solid tumors segregated by panCK+ PD-L1+ expression, respectively. **F.** Correlation of panCK PD-L1+ expression and PD-L1 expression in Treg cells (CD3+CD4+FoxP3+), T helper cells (CD3+CD4+FoxP3-), cytotoxic T cells (CD3+CD8+) and αSMA+ cells. Correlation values (r^2) are shown. **G., H.,** and **I.** PD1+ Thelper cells (CD3+CD4+FoxP3-PD1+), PD1+ cytotoxic T cells (CD3+CD8+PD1+) and PD1+ Treg cells (CD3+CD4+FoxP3+PD1+) in the 3 subcategories of solid tumors segregated by panCK+ PD-L1+ expression, respectively. In all panels each symbol is the mean of 3 ROIs per tumor. The means ± SEM are shown for each group. Students T test, unpaired. Statistically significant differences are noted. All p values shown are significant based on Benjamini-Hochberg control for false discovery at an alpha of 0.05.
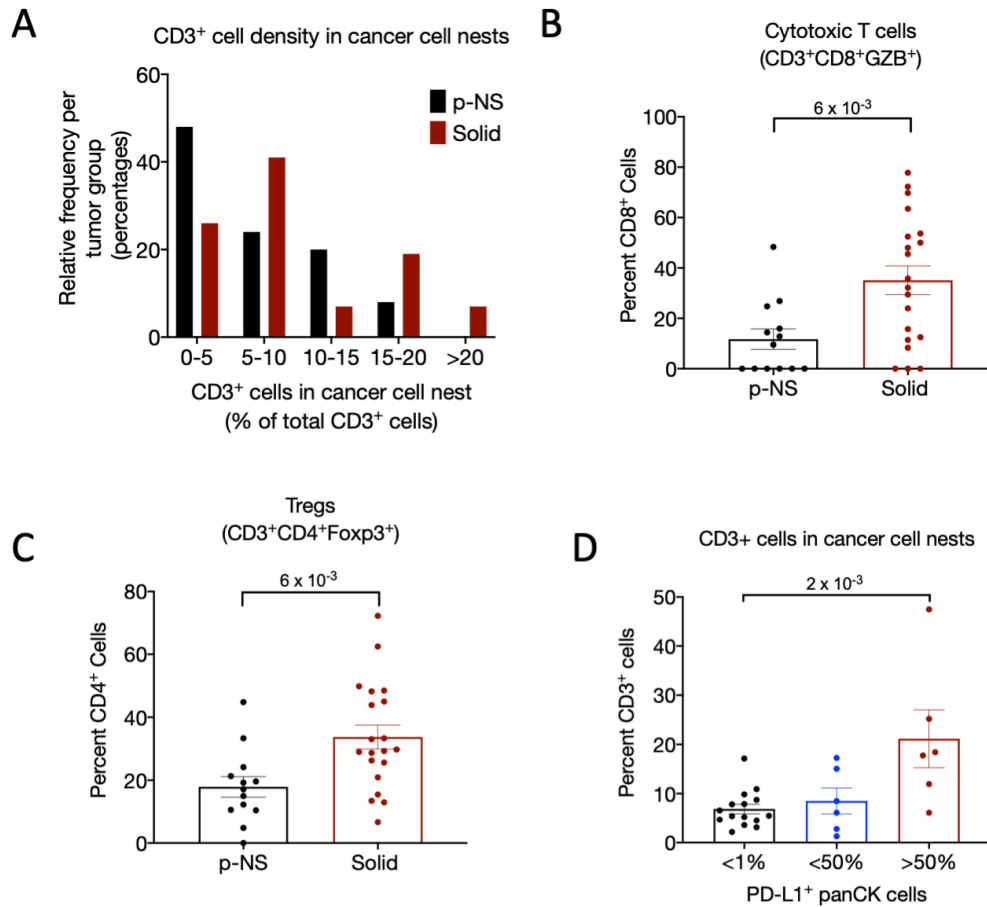
Figure 6. Distribution of T cells among cancer cell nests **A.** Frequency distribution of p-NS and solid tumors based on percent of T cells located within the cancer cell nests. **B.** Cytotoxic T cells (CD3+CD8+) within the cancer cell nests as a percent of CD3+ cells in the tumor. **C.** Tregs (CD3+CD4+FoxP3+) within the cancer cell nests as a percent of CD4+ cells in the tumor. **D.** T cells (CD3+) within the cancer cell nests as a percentage of total T cells in the 3 subcategories of solid tumors segregated by panCK+ PD-L1+ expression. In all panels B,C & D, each symbol is the mean of 3 ROIs per tumor, and the means ± SEM are shown for each group. Students T test, unpaired. Statistically significant differences are noted. All p values shown are significant based on Benjamini-Hochberg control for false discovery at an alpha of 0.05.
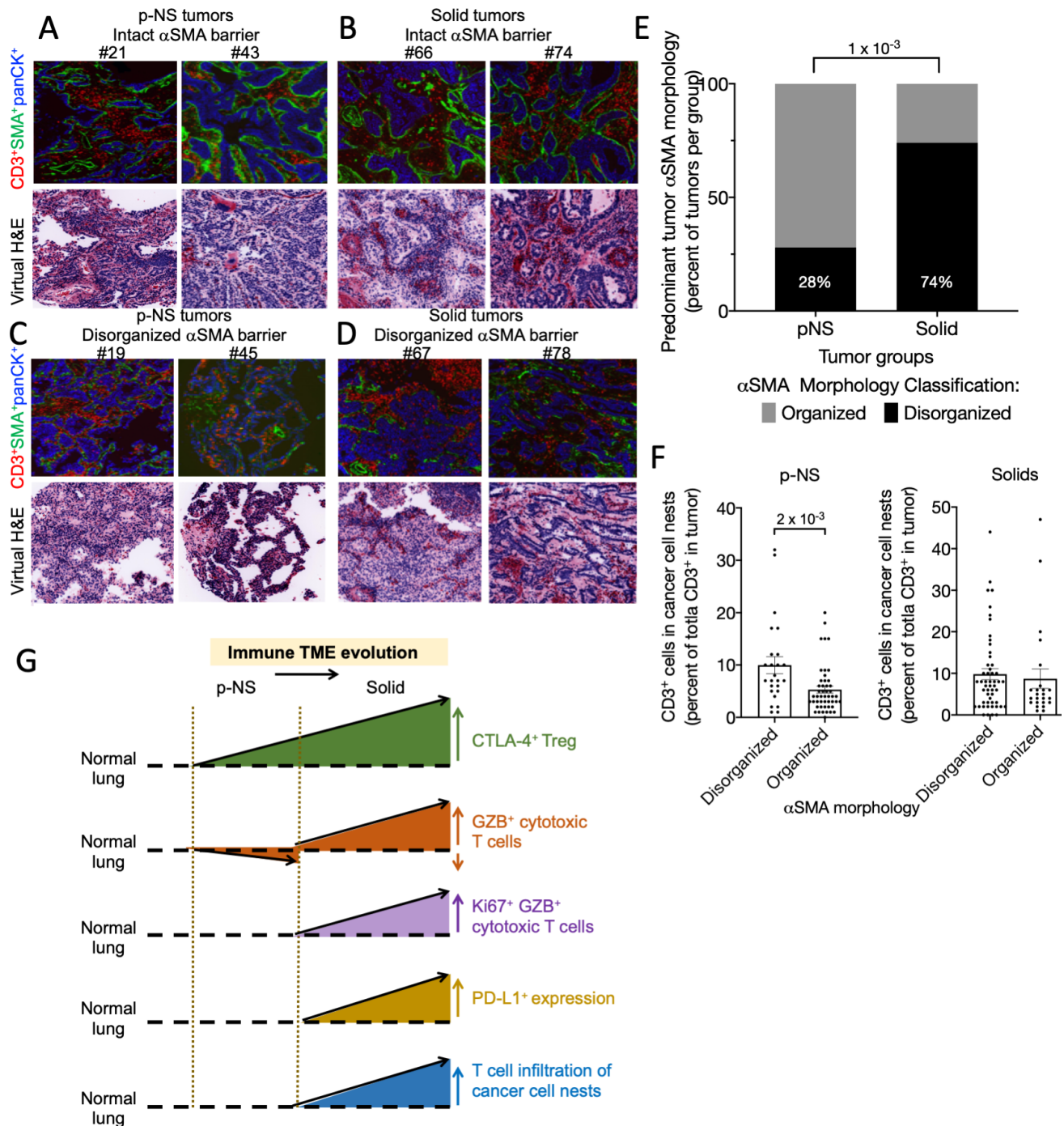
Figure 7. Relationships between tumor stroma and cancer cell nests. A. Immunofluorescence and corresponding virtual H&E of two p-NS tumors with an intact αSMA barrier, **B.** two solid tumors with an intact SMA barrier; **C.** two p-NS tumors with a disrupted SMA barrier; **D.** two p-NS tumors with a disrupted αSMA barrier. All images acquired at 200x magnification. **E.** Predominant tumor αSMA morphology by tumor group. p value, Fischer's Exact test. **F.** CD3+ cell infiltration of cancer cell nest per ROI grouped by αSMA morphology of the ROI. Left are p-NS tumors and right Solid tumors. Statistically significant differences are noted. Unpaired Student's T test. **G.** Model for evolution of immune TME is stage 1A NSCLC. See text for discussion. Vertical dotted lines are separation between p-NS and Solid groups.

Supplemental Table I: Clinical Characteristics

A.

	p-NS Mean (range) n=25	Solid Mean (range) n=27	p value
Age	69 (53-83)	73 (54-86)	ns
Sex	17 Female 8 Male	16 Female 11 Male	ns
Smoking (Pack years)	25 (0 - 110)	41 (0 - 130)	ns
CT Tumor size (cm)	1.75 (1.1 - 2.8)	1.70 (0.7 – 3.0)	ns
Path Tumor size (cm)	1.48 (0.6 - 2.5)	1.94 (1.1 – 3.0)	0.002
SUVmax	1.34 (0-6.0)	6.88 (0-19.6)	0.001

B. Oncogenic Drivers (% of group)

EGFR	7 (28)	3 (11)
Kras	7 (28)	10 (37)
Braf	0 (0)	3 (11)
Unknown	8 (32)	10 (37)
Not Tested	3 (12)	1 (3)

Table I. A. Subject profiles. B. Mutation status.

Supplemental Table II Profiling Markers

A. Antibody panel:

panCK	PD1	CD209	Arginase
CD3	PD-L1	HLA-ABC	Ki67
CD4	TIM3	HLA-DR	
FoxP3	CTLA-4	αSMA	
CD8	CD19	CD45RO	
GZB	CD68	IDO	

B. Cell types defined by Multiplex IF:

CD3$^+$	T cells
CD3$^+$CD4$^+$	CD4+ cells
CD3$^+$CD4$^+$FoxP3$^+$	Treg cells
CD3$^+$CD4$^+$FoxP3$^+$CTLA-4$^+$	Activated Treg cells
CD3$^+$CD4$^+$FoxP3$^-$	T helper cells
CD3$^+$CD8$^+$	Cytotoxic cells
CD3$^+$CD8$^+$GZB$^+$	Activated cytotoxic T cells
CD3$^-$CD68$^+$CD209$^-$	Macrophages
CD3$^-$CD68$^-$CD209$^+$	Dendritic cells
αSMA+CD3-panCK-	Fibroblasts
panCK+	Cancer cells/epithelial cells

C. Other markers:

PD1	Checkpoint receptor
PD-L1	PD1 Checkpoint ligand
TIM3	Checkpoint ligand
HLA-ABC	MHC class I
HLA-DR	MHC class II
CD45RO	Memory cells
IDO	Immune suppression, tryptophan catabolic enzyme,
Arginase	Immune suppression, Arginine catabolic enzyme

Table II. A. Antibody panel; B. Cell types assignments; C. Activation and other markers.